ELSEVIER

Contents lists available at ScienceDirect

Weather and Climate Extremes

journal homepage: www.elsevier.com/locate/wace



Mesoscale patterns associated with two distinct heatwave events in coastal Santa Barbara, California, and their impact on local fire risk conditions

Gert-Jan Duine a,*, Leila M.V. Carvalho a,b, Charles Jones a,b

- a Earth Research Institute, University of California, Santa Barbara, USA
- b Department of Geography, University of California, Santa Barbara, USA

ARTICLE INFO

Keywords: Heatwaves Mesoscale processes Temperature extremes Wildfires Mountain waves Southern California

ABSTRACT

This study investigates mesoscale mechanisms associated with two extreme heatwayes affecting Santa Barbara County (SBC), southern California, and their implication for severe fire weather. We examine these issues using a database consisting of surface stations, radiosoundings, and 1 km grid spacing simulations with the Weather Research & Forecasting (WRF), including a climatology spanning 32 years. During the first heatwave event, synoptic conditions induced downslope winds on the southern-facing slopes of the Santa Ynez Mountains (SYM) on July 6, 2018. One surface station hit an all-time record, and nine surface stations exceeded 99.9th percentiles of surface temperatures. A wildfire (the Holiday Fire) erupted on the slopes of the SYM driven by high temperatures, low relative humidity, and strong winds. The nearby radiosonde registered temperatures at 850 hPa that exceeded the 95th percentile historical records (62 yrs). WRF simulations indicated that mountain wave activity contributed to the excessive surface temperatures on the south-facing slopes of the SYM, and explained the late evening timing for the maximum daily temperatures. The second heatwave broke all-time temperature records at 10 surface stations across SBC on September 6, 2020. Maximum temperatures for most of the SBC occurred during mid-afternoon, the highest observed temperature at the surface was 48.3 $^{\circ}\mathrm{C}$ (118.9°F), and the 850 hPa temperatures exceeded the 99th percentile. The September 2020 event occurred under weaker synoptic forcing (pressure gradients) than the July 2018 event, resulting in weaker winds in coastal Santa Barbara (including the slopes of the SYM) and Santa Ynez Valley. Nonetheless, the extreme heat and low relative humidity increased the Fosberg Fire Weather Index (FFWI) at critical values for a few hours in some sites when winds were moderate. To evaluate the relative importance of these extreme events in the historical context and to assess the region's wildfire risk we propose a novel diagram based on the joint behavior of winds, temperature, humidity and FFWI. While no wildfires have broken out during the September 2020 heatwave, our analysis suggests that a combination of extreme heat with stronger winds would lead to unprecedented fire danger. These extreme conditions may become more common in a warming planet.

1. Introduction

Heatwaves are among the most disruptive environmental risks for humanity and the environment. These events impact health and mortality (Robine et al., 2008; Ostro et al., 2009), can affect natural environments and crops (Sun et al., 2019), increase water stress and wildfire danger (Sutanto et al., 2020; Jyoteeshkumar reddy et al., 2021). Heatwaves occur all over the world, and are becoming more frequent due to global warming (Perkins-Kirkpatrick and Lewis, 2020; Dosio et al., 2018). Understanding regional-to-local impacts of heatwaves will contribute to a more resilient society to climate related disasters

Mechanisms and processes that influence heatwaves exist on multiple temporal and spatial scales and thus vary by region (Adams et al., 2020). They are often associated with specific synoptic scale patterns (Grotjahn et al., 2016), and may follow the buildup of high pressure aloft under which tropospheric heat accumulates (Miralles et al., 2014; Thomas et al., 2020). Intraseasonal oscillations such as the Madden–Julian Oscillation (MJO) (Moon et al., 2011), and soil desiccation after a period of drought (Miralles et al., 2014; Zeppetello et al., 2022) are features relevant to development of heatwaves. On synoptic scale, heatwaves in the U.S. have been more associated with 500 hPa geopotential height anomalies and anticyclonic flows rather than MSLP anomalies (Adams et al., 2020). Nevertheless, prolonged droughts may influence heatwaves in the western US, thereby increasing wildfire risk (Williams et al., 2019), partly due to decreased moisture availability leading to dry fuel beds (Pellizzaro et al., 2007).

^{*} Correspondence to: Ellison Hall, UC Santa Barbara, Santa Barbara, CA 93106, USA. E-mail address: duine@eri.ucsb.edu (G.-J. Duine).

Santa Barbara County (SBC) in southern California exhibits unique topographic features that induce significant gradients in temperatures, humidity, and winds (Jones et al., 2021). Coastal Santa Barbara extends from the southern-facing slopes of the Santa Ynez Mountains (SYM) in southern California toward the cool Pacific Ocean (Fig. 1). Consequently, the diurnal and seasonal cycles of temperature are strongly moderated by the influence of the ocean (Zigner et al., 2021). The SYM (elevation ~1000 m MSL) and the San Rafael Mountains (SRM, elevation ~2000 m MSL) merge on the eastern portion of the east—west oriented coast, forming the V-shaped Santa Ynez Valley (SYV) that is typically much hotter and drier than the coast (Fig. 1). Despite its relatively mild weather year-round, extreme events occur occasionally, and range from extreme winds (Zigner et al., 2021) to heavy precipitation events (Nash and Carvalho, 2020; Oakley et al., 2018).

Zigner et al. (2021) examined all available station records on the slopes of the SYM, and showed that extreme temperature events are sometimes accompanied by strong and dry downslope winds — locally known as Sundowner winds or Sundowners (Blier, 1998; Cannon et al., 2017; Jones et al., 2021; Zigner et al., 2021). These events have been correlated with enhanced MSLP gradients over the Santa Barbara (SBA) area (Jones et al., 2021) and the presence of mountain waves (Carvalho et al., 2020). In some occasions, Sundowners related to adiabatic warming and transport of hot and dry air associated with mountain wave activity (Carvalho et al., 2020; Duine et al., 2019, 2021), may cause further increase in surface temperatures and decrease in relative humidity. Another unique feature of Sundowners is that these winds exhibit three distinct regimes (Jones et al., 2021): western Sundowners (dominant north-northwest wind direction with strong magnitudes on the western portion of the SYM), eastern Sundowners (dominant north-northeast winds, with high magnitudes on the eastern portion of the SYM) and a combination of both regimes. Particularly in the summer, when hot and dry air masses dominate, temperatures during Sundowners can exceed 35 °C in the evening hours after sunset (Blier, 1998; Zigner et al., 2021). Although these extreme temperature events are rare and short-lived, they pose a challenge to the local population as they have a profound effect on human comfort and the environment, and significantly increase wildfire risk. More importantly, the combination of the mountainous terrain combined with the frequent Sundowner winds place Santa Barbara among the most vulnerable fire prone regions in Southern California (Zigner et al., 2020; Murray et al.,

The severity of an extreme event dramatically increases when it occurs as a compound event, i.e. two (or more) extremes occurring at the same time (Zscheischler et al., 2021). Examples of compound events are a combination of atmospheric heat and drought (Feng et al., 2020), or hot, dry windy conditions combined with low fuel moisture (Jyoteeshkumar reddy et al., 2021). Here, we consider the compound extreme event when atmospheric conditions are characterized by regional hot air masses combined with conditions of strong MSLP gradients, conducive to Sundowner winds. Our rationale is that these compound extreme events significantly increase the probability of critical fire weather in the region, increasing the risk of fast spreading wildfires (Zigner et al., 2020). To investigate the relative impact of these extreme conditions on critical fire weather, we examine two extreme temperature events. The first event occurred on July 6, 2018, associated with temperatures exceeding 35 °C and accompanied by strong Sundowner winds reaching 16.1 m s⁻¹ (sustained winds) and 23.7 m s⁻¹ (gusts) that reached coastal plains well within populated areas. A wildfire ("the Holiday fire") broke out in a populated community living in the wildland urban-interface on the southern slopes of the SYM, and rapidly spread on the evening of July 6 driven by strong gusty winds accompanied by high temperatures. The second extreme event occurred in September of 2020, but in this case light winds were present in most locations, and moderate winds (sustained winds of 13.9 m s⁻¹ and gusts of 18.3 m s⁻¹) were restricted to the upper slopes of the SYM. The hottest day during this heatwave was September 6, during which

several stations broke all-time temperature records, with the highest recorded temperature of $48.3~^{\circ}\text{C}$ (118.9°F) in the SYV. Although no wildfire broke out in SBC during this period, it is worth noting that at least three wildfires (El Dorado, Valley and Bobcat) did break out in Southern California early September.

As heatwaves and record-breaking temperatures may continue in frequency at alarming pace, understanding regional impacts of these events is imperative to mitigate the effects of global warming and increase preparedness for climate related disasters. Compound events may become more frequent and recognizing their main characteristics is relevant for decision making. The main objective of this article is to discuss these two extreme events with respect to the climatology and evaluate their potential in enhancing wildfire risks in a fire prone region with complex topography. Here we investigate the meteorological processes leading up to these two distinct heatwaves that resulted in regional record-breaking temperatures. We discuss differences and commonalities between these two heatwave events focusing on mesoscale processes and implications for extreme fireweather. More specifically, this paper addresses the following research questions:

- (1) What are the main mechanisms driving these two heatwaves?
- (2) What are the similarities and differences between the two heat-waves?

The paper is organized as follows. Section 2 discusses the data and methods used, including observations, mesoscale simulations, the definition of fire weather metrics and the selection of the heatwave events. Sections 3 and 4 explore the mesoscale mechanisms involved in the heatwaves of July 6 2018 and September 6 2020, respectively. We present a novel wildfire diagram in Section 5 that uses historic data to analyze the fire weather risk based on atmospheric conditions in present times. We conclude the study in Section 6.

2. Data and methods

2.1. Observations

We used a combination of U.S. Forest Remote Automated Weather Stations (RAWS) and Automated Service Observations Stations (ASOS) (Fig. 1 and Table 1). The RAWS report 10-minute averages of winds (from 3 s samples), temperature and humidity on an hourly frequency, wind gusts represent the highest sampled wind speed in the preceding hour. RAWS observe temperature and wind at 1.2 to 2.4 m agl, and winds at 6.1 m agl. ASOS report 2 min averages from 5 s sampling rate on a sub-hourly frequency, with observations of temperature and humidity at 2 m agl, and winds at 10 m agl. For this study, these averaged values were used, and, when compared directly to model output, the values closest to the full hour were used. The stations have a different data coverage, largely depending on installation date (Table 1). Stations that have been installed for less than 5 yrs were not considered for climatological context.

Radiosonde data at Vandenberg (KVBG, Fig. 1) was obtained from the Integrated Global Radiosounding Archive (IGRA) at the National Climate Data Center (NCDC) (September 1958–2020). For better comparison among the soundings, we only considered the 00:00 UTC (17:00 PDT, close to the time of maximum warming) soundings: 1510 soundings in July and 1443 soundings in September. Physically unreliable outliers (i.e., temperatures above 50 °C and below -50 °C) were discarded.

We define daily maximum temperature T_{max} as the highest recorded temperature for a given day in local time Pacific Daylight Time (PDT = UTC - 7). For surface stations the full datasets were used for percentile computation. For radiosonde data we have computed percentiles using monthly data.

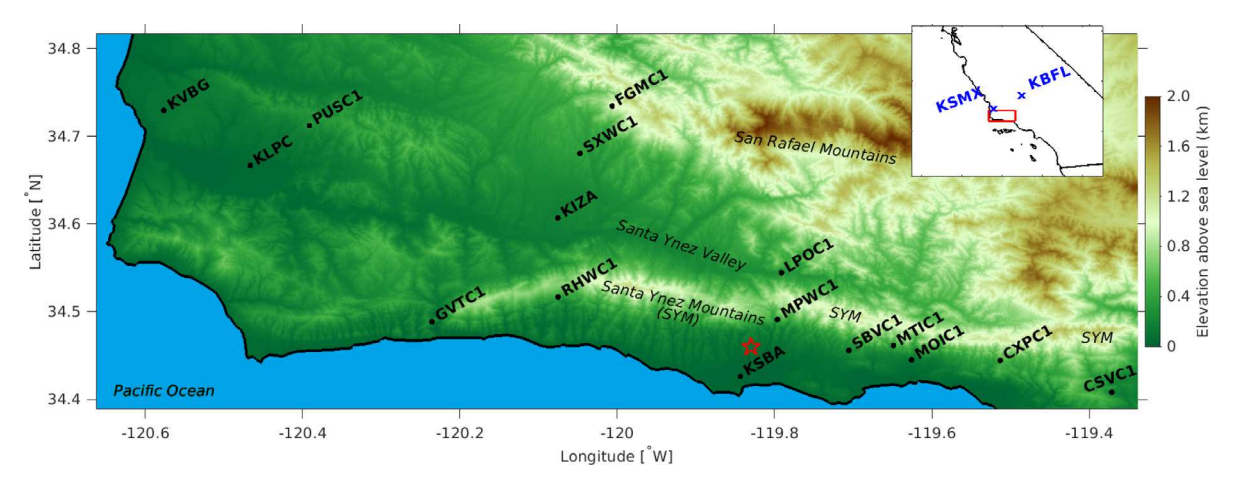


Fig. 1. Stations used in this study for analysis across the study area, plotted on top of the terrain elevation. The inset map indicates the relative position of the study area in Southern California, and includes the KBFL and KSMX stations. The red star indicates the approximate ignition location of the Holiday fire.

Table 1
Stations, elevation, data coverage and type of stations.

Station ID	Geography description	Elevation [m]	Data start	Date end	Туре
CXPC1	Eastern SYM - middle slopes	539	Apr. 2019	Sep. 2020	RAWS
FGMC1	San Rafael Mountains	970	Nov. 2011	Sep. 2020	RAWS
GVTC1	Western SYM - middle slopes	268	Jan. 2018	Sep. 2020	RAWS
KBFL	Central valley	155	Oct. 1998	Sep. 2020	NWS/ASOS
KIZA	Santa Ynez Valley - center	205	Sep. 2009	Sep. 2020	NWS/ASOS
KLPC	Santa Ynez Valley - coastal	27	Nov. 1999	Sep. 2020	NWS/ASOS
KSBA	Coastal plain	3	Oct. 1998	Sep. 2020	NWS/ASOS
KSBP	Coastal	63	Nov. 1998	Sep. 2020	NWS/ASOS
KSMX	Santa Ynez Valley - northwest	74	Oct. 1998	Sep. 2020	NWS/ASOS
KVBG	Santa Ynez valley - coastal	112	Oct. 1998	Sep. 2020	NWS/ASOS
LPOC1	Santa Ynez valley - center	299	Dec. 1999	Sep. 2020	RAWS
MOIC1	Eastern SYM - foothills	87	Apr. 2011	Sep. 2020	RAWS
MPWC1	Center SYM - middle slopes	455	Jul. 2015	Sep. 2020	RAWS
MTIC1	Eastern SYM - middle slopes	494	Dec. 1999	Sep. 2020	RAWS
RHWC1	Western SYM - middle slopes	447	Jul. 2015	Sep. 2020	RAWS
SBVC1	Eastern SYM - foothills	230	Jun. 2011	Sep. 2020	RAWS
SXWC1	Santa Ynez Valley - slopes	427	May 2017	Sep. 2020	RAWS

2.2. Mesoscale simulations

Mesoscale mechanisms were investigated with the Weather Research & Forecasting (WRF) model version 4.0.1 (Skamarock and Klemp, 2008) using the configuration described in Duine et al. (2019). ECMWF Reanalysis ERA5 input data on a 31 km grid spacing were used for model initialization and boundary conditions (Hersbach et al., 2020). We used four two-way nested grids to dynamically downscale from 27 km to 1 km using 55 vertical sigma levels and a model top at 50 hPa. Grid nudging was applied in the outermost domain on a 6-hr interval. Physical parameterizations included the Mellor-Yamada-Nakanishi-Niino level 2.5 (MYNN) (Nakanishi and Niino, 2006) for the planetary boundary layer (PBL) - together with the recommended surface layer scheme - and the Noah land surface model (Tewari et al., 2004) was used after adopting higher values of roughness length (z_0) with the same procedure as in Cao and Fovell (2018); this approach also improved surface wind characteristics during Sundowner conditions (Duine et al., 2019). Other subgrid parameterizations used can be found in Duine et al. (2019). This configuration successfully simulates mountain wave dynamics associated with Sundowners (Carvalho et al., 2020). We used the 32-yr WRF downscaling dataset (hourly, 1 km grid spacing) described in Jones et al. (2021) to derive meteorological variables (e.g., MSLP differences) for climatological context. Validations of this data set against stations are discussed in Jones et al. (2021).

The simulations for July 6 2018 heatwave were initialized on July 3 2018 18:00 UTC and integrated for 126 h. The simulations for

the September 2020 heatwave were initialized on September 3 2018 18:00 UTC and integrated for $126\ h.$

2.3. Fire weather index

We used the Fosberg Fireweather Index (FFWI) to evaluate the impacts of these events on fire weather risk (Fosberg, 1978). FFWI computes the potential influence of weather on a wildfire based on current relative humidity, temperature and wind speed (Goodrick, 2002), and is defined as:

$$FFWI = \eta \sqrt{1 + U^2} \tag{1}$$

where U is wind speed in mph, and η is the moisture damping coefficient, defined as:

$$\eta = 1 - 2(m/30) + 1.5(m/30)^2 - 0.5(m/30)^3$$
 (2)

The equilibrium moisture constant m is a function of temperature in degree Fahrenheit (T_f) and relative humidity RH in percent:

$$m = \begin{cases} &\text{for } RH \le 10\% : \\ &0.03229 + 0.281073RH - 0.000578RH \ T_f \\ &\text{for } 10\% < RH \le 50\% : \\ &2.22749 + 0.160107RH - 0.01478T_f \\ &\text{for } RH > 50\% : \\ &21.0606 + 0.005565RH^2 - 0.00035RH \ T_f - 0.483199RH \end{cases}$$
 (3)

Large values of FFWI indicate large flames and rapid fuel drying; FFWI values exceeding 25 are considered severe in chaparral ecosystems (Moritz et al., 2010), and higher than 50 are considered as critical fire weather on a national scale (Goodrick, 2002; Zigner et al., 2021). FFWI has been used to indicate wildfire threats using direct model output (Jones et al., 2010; Williams et al., 2019), and observations (Zigner et al., 2021). Note that, since both case studies presented in this study were during a prolonged summer drought, we have not considered using the modified FFWI that includes precipitation history (Goodrick, 2002).

We focused the fire weather analysis on observations from stations. We composed fire weather diagrams by averaging values for FFWI and RH. Values for FFWI and RH were averaged for the observed temperatures and wind speeds for available measurement periods (Fig. 1) using 2 °C and 2 m s $^{-1}$ bin increments. Thus, for each bin of wind speed and temperature, one average value for all available observed FFWI and RH was computed. The resulting diagrams are used to compare historically observed wildfire risks with the two events analyzed here.

2.4. Definition of heatwaves and selection of events

Many different definitions of heatwaves exist, and depend on the regional and local climate, local infrastructure and health demands (Gershunov et al., 2009). The US National Weather Service (NWS) defines a heatwave as "a spell of abnormally and uncomfortably hot and unusually hot weather". In the western U.S., a heatwave is defined if temperatures reach 100 F (37.8 °C) for three or more consecutive days. Previous studies employed three consecutive days above the 90th or 95th percentiles (Dosio et al., 2018; Perkins-Kirkpatrick and Lewis, 2020).

In both events investigated in this paper, T_{max} exceeded the 99th percentile for three consecutive days in most stations (supplemental Table S1). The highest temperatures for each event were reported on July 6 2018 and September 6 2020, respectively. These temperatures broke records at the time of their respective heatwave event. However, during the September heatwave the observed T_{max} broke these previous records (except at MOIC1), indicating the extreme and distinct nature of both events. While placing these two events into the regional historical context is limited to the relatively short and variable length of the records, these days unquestionably represent two extreme conditions. Here we investigate in detail their climatological importance and spatiotemporal variability.

3. July 6 2018 'Holiday Fire': heatwave and Sundowner winds

3.1. Overall characteristics from surface stations

The NWS in Oxnard (NWS/LOX) issued a fire weather watch on July 3 at 15:00 PDT, followed by a red flag warning on July 5 2018 at 09:50 PDT (Dave Gomberg, NWS/LOX, personal communication). The Holiday fire broke out in northern Goleta on July 6 at 20:40 PDT. Despite the extreme fire weather conditions, thanks to the accurate forecast and close collaboration between the NWS/LOX and the Santa Barbara County Fire Department, this wildfire was quickly contained, preventing its spread toward populated areas in the city of Goleta. The Holiday fire burned an area of 113 acres, destroyed 10 single family homes and was completely contained on July 10, 2018.

On July 6, the day with highest temperatures, T_{max} in most stations reached similar values of around 40 °C or higher (Table 2 and Fig. S1 in supplemental material). T_{max} exceeded the 99.9th percentile in most stations, indicating the extreme nature of the July 6 2018 heatwave. T_{max} at MOIC1 (foothills, eastern SYM) broke the all-time record. We further emphasize that the KBFL station, located in the San Joaquin valley (Fig. 1), reported T_{max} of 37.0 °C (98.6°F), above 97th percentile. On average, KBFL was closer to normal temperatures for July than the other stations in the study area (compare Figs. S2a and S2c). This

suggests that the heatwave was more extreme in the SBC than in the San Joaquin valley.

The timing for T_{max} varied considerably among the stations (Table 2), and indicates distinct mechanisms during the heatwave. In the western part of the SYM (RHWC1), T_{max} of 40.6°C (105.1°F) was reached around 14:00 PDT with NW winds (5.8 m s⁻¹) and T_d of 6.0 °C. The MPWC1 (central slopes of the SYM) reported T_{max} (41.7 °C or 107.1°F) at 15:06 PDT with westerly winds of similar strength. Further east, on the slopes of the SYM, T_{max} values at SBVC1 and MOIC1 were slightly higher (42.8 and 42.2 °C, respectively) at 18:00 PDT and accompanied northerly winds. The latest T_{max} occurred at KSBA (38.0 °C (100.4°F) at 20:00 PDT) with northerly winds. The stations on the eastern SYM south-facing slopes (SBVC1, MOIC1, KSBA) showed atypical temperature diurnal cycles for July, since the local sunset is around 20:00 PDT (Zigner et al., 2021). Humidity at these stations was near single digits. In the SYV, north of the SYM, a large westeast gradient of T_{max} (up to 15.9 °C) was observed (Table 2). Within the valley KVBG (coastal) reached T_{max} of 28.5 °C (83.3°F) whereas within KIZA (center) reached T_{max} of 41.0 °C (105.8°F) at 14:00 PDT, also accompanied by NW wind. Further east in the narrower portion of SYV at LPOC1, T_{max} reached 44.4 °C (111.9°F) at around 14:35 PDT. Section 3.3 discusses the mechanisms related to the timing of T_{max} for both SYM south-facing slopes and the SYV.

3.2. Synoptic forcing

The synoptic conditions leading to the heatwave and Sundowner event of July 6 2018 were characterized by a combination of intense heat over continental U.S., the eastward propagation of an extratropical cyclone and the enhancement of pressure gradients off the coast of Santa Barbara (Fig. 2). From July 3-4, lower-tropospheric (850 hPa) high temperatures (above 30 °C) were observed over large portions of the U.S., particularly over the Interior West (Figs. 2a, b). On July 5 (Fig. 2c), pressure gradients began to increase off the west coast, driven by a significant lowering in pressure near Baja California (a thermal low). With the continuous heat, this low pressure system intensified and extended toward southern California on July 6 (Fig. 2d). Meanwhile, decreasing strength of the low pressure system off the coast of Washington (Figs. 2a-c), resulted in the increase of pressure gradient off the coast of California (Fig. 2d). Given the east-west orientation of the Santa Barbara coast, these pressure gradients were such that they encouraged northerly cross-mountain winds to develop. Over the SBA area, MSLP differences strengthened to -5.4 hPa (KSBA minus KSMX) and -6.0 hPa (KSBA minus KBFL) on July 6 (see supplementary Figure S3).

Negative values for both MSLP differences of such observations are associated with winds perpendicular to the SYM range, and are considered large enough for the development of strong Sundowner winds on the south-facing of the SYM (Sukup, 2013; Carvalho et al., 2020). Based on 32-yr of WRF simulations (Jones et al., 2021), these values exceeded the 99.9th (KSBA minus KSMX, Fig. S4a), and 99.0th percentiles (KSBA minus KBFL, Fig. S4b).

3.3. Mesoscale forcings

3.3.1. Observations

Stations in the valley, mountains and coast exhibited distinct diurnal cycles during this event (Fig. 3). In the morning winds over land were weak in most stations, with exception of the western middle slope RHWC1 (Fig. 3b, e). The valley stations exhibited an afternoon peak in winds and temperatures with KIZA (central SYV) and LPOC1 (eastern SYV) reaching 40 °C around 14:00 PDT (Fig. 3a, b). However, locations closer to the coast line (KVBG) exhibited a decline in temperature in the afternoon (Fig. 3a), most likely due to the intensification of the sea breeze (Fig. 3b).

Table 2 Observations of T_{max} (°C) with percentile exceeded in parenthesis, T_{max} (°F), dew point temperature (T_d), relative humidity (RH) and winds (wind, gust and wind direction) at time of T_{max} for a selection of surface stations on July 6 2018. See Fig. S1 for a spatial map.

Station	Elevation (m)	<i>T_{max}</i> (°C)	<i>T_{max}</i> (°F)	T_d (°C)	RH (%)	Wind (gust) (m s ⁻¹)	Wdir (°N)	Time of T_{max} (PDT)
MOIC1	87	42.2 (100.0)	108.0	1.6	8.0	3.1 (9.4)	001	18:07
LPOC1	299	44.4 (99.9)	111.9	6.4	10.0	2.2 (7.2)	276	14:35
SBVC1	230	42.8 (99.9)	109.0	5.1	10.0	3.6 (8.1)	010	17:24
MPWC1	455	41.7 (99.9)	107.1	4.3	10.0	6.7 (10.3)	264	15:06
KIZA	205	41.0 (99.9)	105.8	7.4	12.9	6.7 (9.3)	280	13:55
RHWC1	447	40.6 (99.9)	105.1	6.0	12.0	5.8 (11.6)	324	14:06
FGMC1	970	38.9 (99.9)	102.0	0.7	9.0	1.8 (7.2)	348	14:09
KSBA	3	38.0 (99.9)	100.4	5.3	13.2	2.1 (-)	030	20:00
KSMX	74	33.0 (99.8)	91.4	12.1	27.9	7.7 (-)	300	12:00
KVBG	112	28.5 (99.8)	83.3	11.7	35.4	6.2 (-)	340	11:55
KLPC	27	29.0 (99.7)	84.2	14.0	40.0	8.2 (-)	260	12:00
KBFL	155	37.0 (97.0)	98.6	10.2	19.6	5.7 (-)	300	16:00

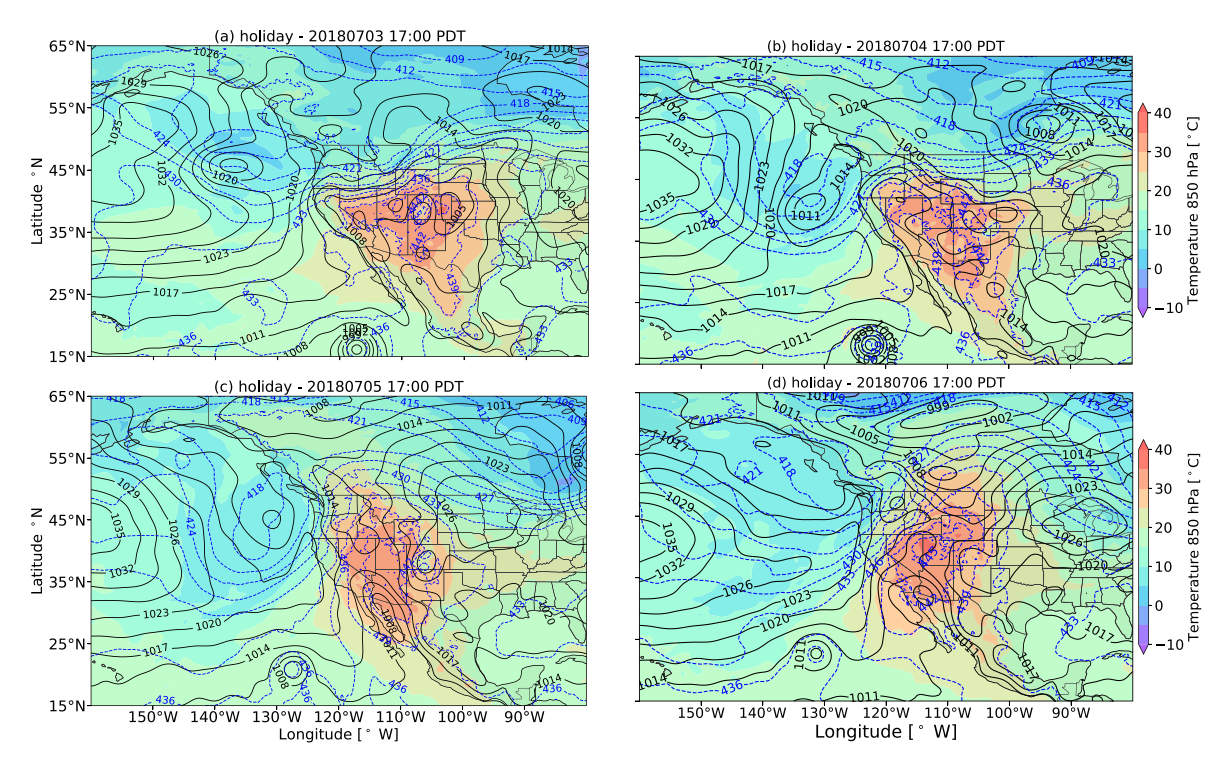


Fig. 2. CFSv2 850 hPa temperatures (colors), MSLP (hPa, black solid contours), and 500–850 hPa thickness (dam, dashed blue contours) during the days leading up to July 6 2018 at indicated times. (For interpretation of the references to color in this figure legend, the reader is referred to the web version of this article.)

Contrastingly, over the south-facing slopes of the SYM, maximum winds were reached after 20:00 PDT, with strongest sustained winds reported at RHWC1 (16.1 m s⁻¹) followed by SBVC1 (13.4 m s⁻¹) (Fig. 3b). The strongest gusts were reported at SBVC1 (23.7 m s^{-1}), followed by RHWC1 (20.1 m s⁻¹) and MOIC1 (15.2 m s⁻¹) (not shown). Note that after 17:00 PDT, south-facing SYM stations (SBVC1, MOIC1) reported the highest temperatures (42.8 °C and 42.2 °C) (Fig. 3d), whereas stations in the SYV (KIZA, LPOC1) and RHWC1 indicated progressive cooling (Fig. 3a, d). Moreover, the SBVC1 and MOIC1 stations exhibited a sharp decrease in T_d after 17:00 PDT (minimum values of 0.8 °C and -0.2 °C, resp.), consistent with the intensification of downslope winds (Fig. 3e, f). Although the coastal KSBA station located at lower elevations did not show similar increase in winds in the evening (Fig. 3e), the combined increase in temperature (Fig. 3d) and decrease in T_d (from 14.1 °C to below 5.3 °C) were evident (Fig. 3f). Note that temperatures at KSBA and eastern SYM south-facing stations (SBVC1, MOIC1) remained above 35 °C until midnight (Fig. 3d). The combined increase in winds, temperature and decrease of dew point are associated with sudden intrusions of a drier air masses, occur frequently during Sundowner events, and have been linked to mountain wave activity (Carvalho et al., 2020; Duine et al., 2021; Jones et al., 2021).

3.3.2. WRF simulations

Simulations and observations are compared for winds and temperature in supplemental material Figure S5. Differences between simulations and observations were of similar order of magnitude as for previous case studies, and reasons for differences are thoroughly discussed in Cannon et al. (2017), Duine et al. (2019), Carvalho et al. (2020). To further understand mechanisms associated with the observed diurnal cycles, we investigate simulations of winds and temperatures shown in Fig. 4. Simulations indicate that winds in the SYV in the afternoon were predominantly northwesterly, and were driven by a combination of the prevailing NW winds off the coast, the sea breeze and thermally-driven up valley circulation. Stronger winds were observed and simulated in the western SYM (west of -120.05°W) and off the coast around Point Conception, where NW winds of about 10 m s⁻¹ were present. These patterns are largely consistent with the climatology of western Sundowners (Carvalho et al., 2020; Jones et al., 2021; Duine et al., 2021; Zigner et al., 2021). The combined mesoscale processes affected the timing and magnitudes of temperature in the valley in the afternoon. While locations closer to the coast line (e.g., KVBG) reached maximum temperatures early afternoon, locations further inland in the narrower

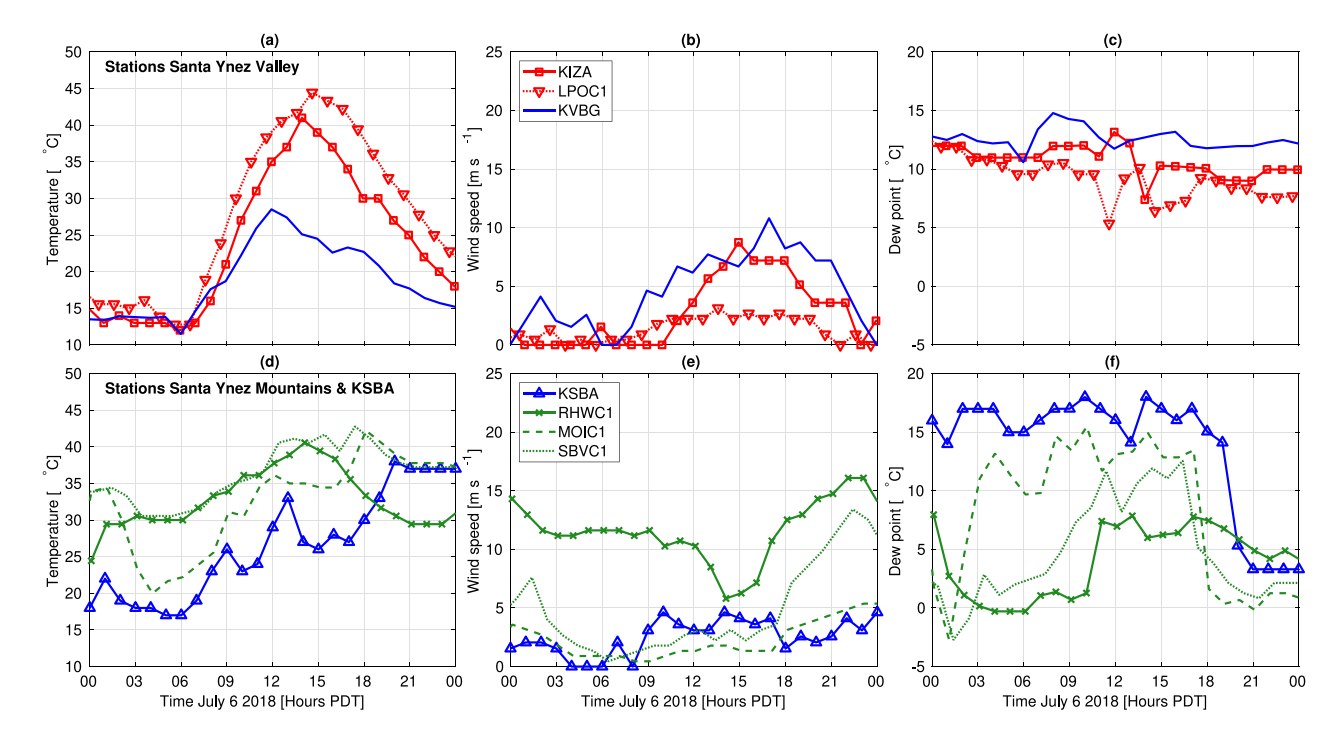


Fig. 3. Observations of (a, d) temperature, (b, e) wind speed, and (c, f) dew points during July 6 2018 for surface stations in (a, b, c) Santa Ynez Valley, and (d, e, f) Santa Ynez Mountains and at KSBA. Colored lines highlight site specifics: red indicates valley stations, blue indicates coastal stations, and green indicates slope and foothill stations in Santa Ynez Mountains. (For interpretation of the references to color in this figure legend, the reader is referred to the web version of this article.)

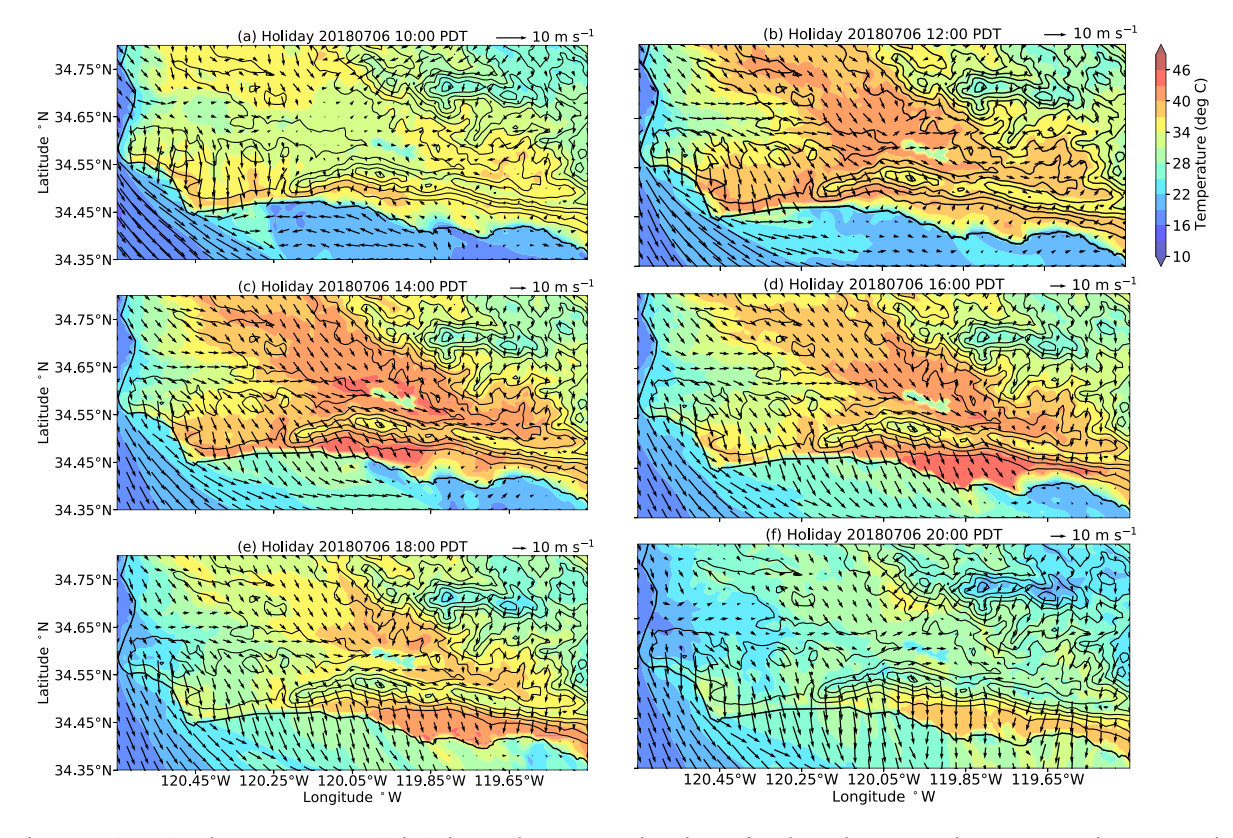


Fig. 4. Winds at 10 m (vectors) and temperature at 2 m (colors) during July 6 2018 at indicated times for 1 km grid spacing simulations. Contours denote terrain elevation each 200 m. Colorbar in (b) applies to all panels. (For interpretation of the references to color in this figure legend, the reader is referred to the web version of this article.)

parts of the SYV showed maximum temperatures late afternoon which resulted in a west–east temperature gradient along the SYV of more than $15\,^{\circ}$ C, in agreement with observations (Figs. 3b, 4b–d).

In the afternoon, winds enhanced on the southern slopes of the SYM with strength and direction location-dependent (Fig. 4c, d). The highest temperatures were reached at 14:00 PDT on the western SYM slopes

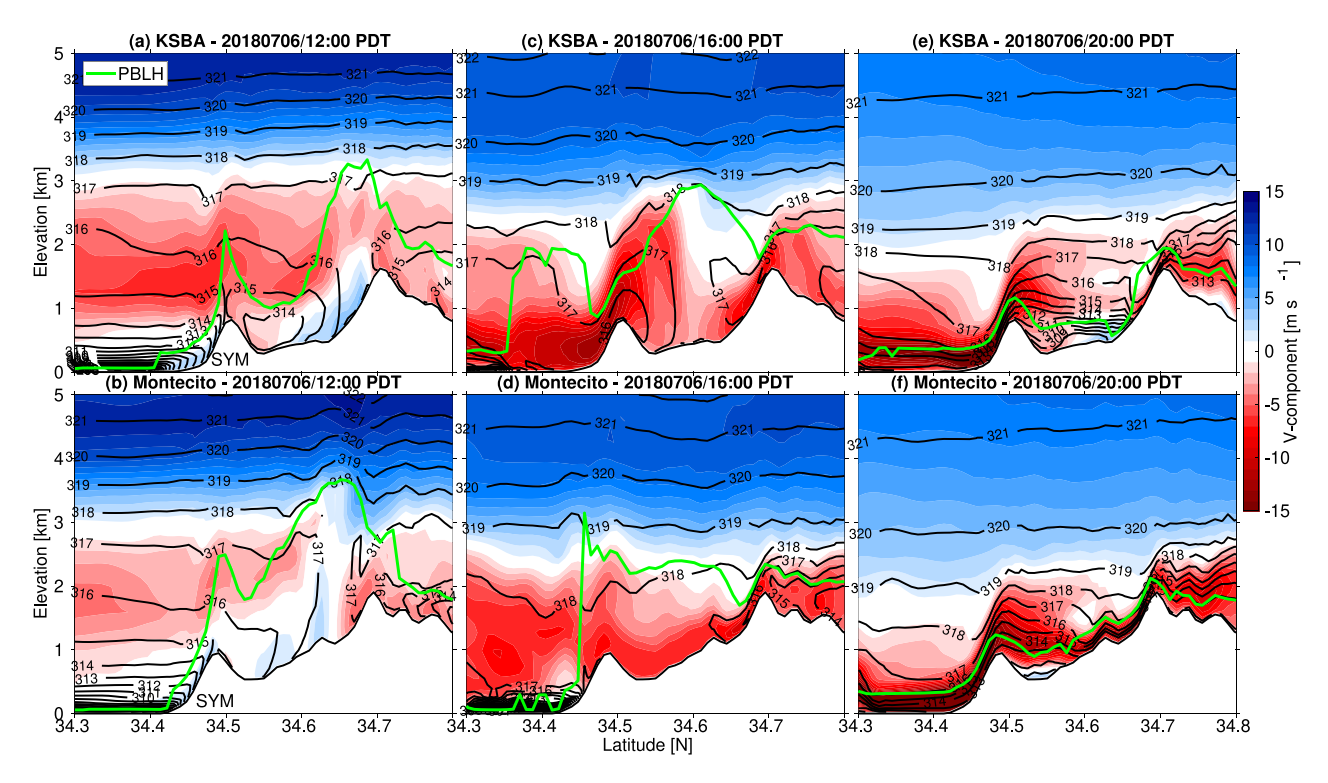


Fig. 5. Vertical cross sections of θ_v , planetary boundary layer height (PBLH, green lines) and meridional wind component (colored shading) during July 6 2018 along KSBA airport and Montecito. SYM is indicated in panels (a, b). (For interpretation of the references to color in this figure legend, the reader is referred to the web version of this article.)

(Fig. 4d), consistent with observations (Fig. 3b). The highest temperatures in coastal areas east of 120°W were simulated at 16:00 PDT and they were significantly higher than the valley at the same time. These high temperatures were observed along with enhanced crossmountain northwesterly winds. Notice that at 18:00 PDT winds were strong along the entire southern slopes of the SYM, with dominantly NNW winds on the western and NNE winds on the eastern portions of the SYM. This was the time of the strongest warming east of 120°W, which affected highly populated areas of Santa Barbara. At 20:00 PDT, winds intensified over central (N-direction) and eastern (NE-direction) SYM, maintaining high temperatures and low moisture on the southern SYM slopes, foothills and coastal areas. Around 20:50 PDT of that day, the Holiday fire broke out sparked by strong winds that resulted in a failure of an electrical conductor. At this time simulated and observed temperatures exceeded 35 °C and winds exceeded 10 m s⁻¹ along the entire coastal SB (Fig. 3d-e, 4f).

To better understand mechanisms associated with these spatiotem-poral patterns of strong winds and high temperatures on July 6, we examine simulated vertical cross sections of virtual potential temperature θ_v , cross-barrier wind (represented by the V-component) and PBL height (relative to MSL, green line) from WRF simulations (Fig. 5). To evaluate dynamical mechanisms explaining the July 6 2018, we focus on cross sections along the middle (across KSBA airport in Goleta) and eastern SYM (across MTIC1 in Montecito), at 12:00, 16:00 and 20:00 PDT.

At noon, a stably stratified marine boundary layer (SSMBL) was present south of the SYM along the KSBA longitude, as indicated by the rapid increase of θ_v with height over the ocean (Fig. 5a). The weak southerly winds advected cooler oceanic air to the southfacing slopes, which explains the relatively low temperatures close to the coastline at this time (Figs. 4b and 3a). In the SYV, convective boundary layer (CBL) processes have initiated the development of a mixing layer, although a stable core was still present. The delay in temperature inversion breakup in the SYV, a feature common to valley environments (Whiteman, 1982), explains partly the relative late timing of T_{max} in the valley at the surface (Fig. 3a). The stable core was

dissolved one hour later (not shown). Thermally driven winds were present in the valley on its northern and southern slopes, indicated by the respective positive and negative values of the V-component (Fig. 5a). The cross section along Montecito (Fig. 5b) shows patterns similar to KSBA (Fig. 5a), except that the stable core was eroded earlier (at 11:00 PDT, not shown), and the CBL was less terrain-following and reached around 3 km msl (Fig. 5b). Along both longitudes, northerly winds were present above the mountaintop (up to 3 km msl). However, winds reversed with height as strong southerly winds were observed in the middle troposphere (Fig. 5a, b), with the cross-barrier wind reaching zero at approximately 3 km msl. This southerly wind was related to the 500 hPa geopotential height pattern shown in Fig. 2. Wind reversals with height have been associated with critical layers that further enhance mountain wave activity (Durran, 1990).

At 16:00 PDT, the level of the cross-barrier winds reaching zero lowered to below 2.5 km msl along both longitudes (Fig. 5c, d). Northerly winds intensified on the south-facing slopes of the SYM along KSBA (Fig. 5c). Along the Montecito cross section, a deep mixed layer (above 2 km MSL) was evident in the SYV in combination with SSMBL on the south-facing slopes of the SYM (Fig. 5d). These results indicate that SSMBL along the KSBA cross section was eroded in the afternoon, while it maintained present across Montecito, explaining the relatively cooler temperatures over eastern coastal SB. The differences in timing of the strong winds and drying along the SYM have been noted to occur frequently (Carvalho et al., 2020), and have been related to the angle of approaching winds north of the SYM (Duine et al., 2021).

At 20:00 PDT, strong downslope winds occurred along both longitudes under the influence of self-induced and mean-state critical layers (Fig. 5e, f). Upstream of the SYM, the convective mixed layer in the SYV in both locations was replaced by a strongly stratified layer. Increased stably stratified air upstream of a mountain range may enhance mountain wave activity (Grubišić et al., 2015; Duine et al., 2021). In addition, the level of the cross-barrier wind component reaching zero lowered to 2 km msl. Thus, at both locations the lee slope winds intensified below a self-induced critical layer in the presence of a mean-state critical layer aloft, and were accompanied by the enhancement of

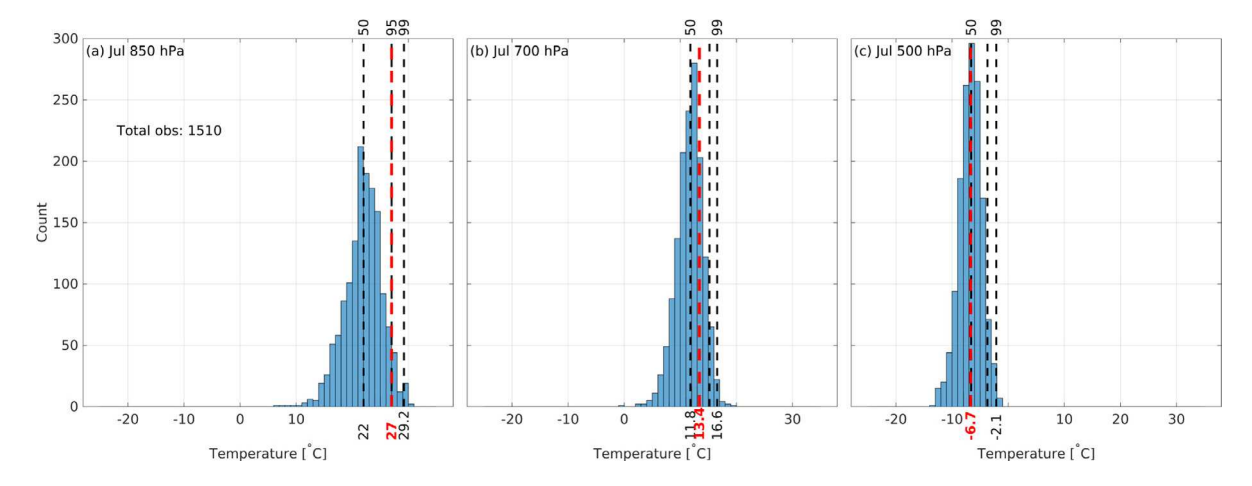


Fig. 6. Histograms of July radiosounding temperatures (17:00 PDT) at (a) 850, (b) 700, and (c) 500 hPa for Vandenberg (KVBG). The red dashed line indicates the observation of July 6 2018, the black dashed lines indicate the 50th, 95th and 99th percentiles for the period of 1958–2020, resp. The total number of observations is indicated in (a). See Fig. 1 for the location of KVBG.

upstream stability and the intensification of MSLP gradient over time (Fig. S3).

3.3.3. Upper-air sounding observations

The cross sections indicate isentropic drawdown above the SYM lee slopes possibly associated with mountain wave activity, which may have contributed to the extreme temperatures and low moisture at the surface. Previous research has shown that the 850 hPa temperature from radiosounding in KVBG upstream (i.e. north) of the SYM is a good indicator of observed temperatures in the lee slopes when mountain waves occurred (Blier, 1998). Along both longitudes in the SYV at 1500 m (around 850 hPa), we find a θ_v of about 316 K (42.8 °C) at 20:00 PDT (Fig. 5e, f). Above the SYM lee slopes (i.e. south of the SYM) this isentrope was located around 500 m agl. The 00:00 UTC (17:00 PDT) radiosounding from KVBG indicated a temperature of 27.0 °C at 850 hPa (red dashed line in Fig. 6a). Air transported adiabatically from 850 hPa to sea level would reach 41.7 °C, consistent with observations, indicating that high temperatures in the lee slopes of the SYM were mainly driven by mountain waves, and consequent adiabatic compression.

We compared the observed temperature sounding at 850 hPa, 700 hPa and 500 hPa on July 6 with the IGRA-KVBG sounding climatology (see Fig. 1 for location). The observed value at 850 hPa (27.0 °C) exceeded the 95th percentiles for July (Fig. 6a), but is less than the respective percentiles for MSLP differences (Fig. S4a) and surface temperatures as observed from stations (99.9th percentile, Table 2). Further aloft, at 700 and 500 hPa, the temperatures of this particular sounding show values closer to the median of the climatological distribution for July (Fig. 6b,c). This indicates that the excessive heat resulted from the combined effect of strong Sundowner winds and associated mountain waves developing in an environment with high temperatures in the lower troposphere and relatively strong MSLP gradients.

4. September 2020 heatwave

4.1. Overall characteristics from surface stations

Although temperatures on July 6 2018 were regarded as extreme, these were exceeded during the heatwave that occurred September 6 2020. Values for T_{max} were at least 4-5 °C higher on September 6 2020 than on July 6 2018 (Table 3 and Fig. S6 in supplemental material). In total, 11 stations in SBC reported record-high temperatures as indicated by the 'percentile' of 100.0. A few surface stations (KSBA, MOIC1 and MTIC1) did not report record-high temperatures, but, these stations

still exceeded the 99.9th percentile (Table 3). We further note that T_{max} at KBFL was 40.0 °C (104°F), thereby exceeding 99.6th percentile (Table 3).

 T_{max} was observed between noon and 16:00 PDT in most surface stations (Table 3), which is in contrast with the July 2018 case when three stations observed T_{max} after 17:00 PDT (Section 3.1). The spatiotemporal variability of T_{max} in the SYV was similar to July 2018 case, with the earliest timing and lowest values of T_{max} in the wider parts of the SYV closer to the coastline (e.g., KVBG reported 33.8 °C, or 92.8°F, at 10:58 PDT). Further east in the SYV (LPOC1), T_{max} of 48.3 °C (118.9°F) was reached the latest of all valley stations (15:35 PDT).

4.2. Synoptic forcing

The days leading up to the September 6 2020 heatwave showed a remarkably different synoptic pattern than during the July 6 2018 heatwave (Fig. 7). A pronounced and persistent ridge dominated atmospheric conditions over most of the western U.S., allowing heat to build up in the lower troposphere, as indicated by increasing temperatures at the 850 hPa level from September 3 to September 6 (Fig. 7). A thermal low pressure area over NW Mexico remained steady in location and intensity during this period. Note that temperatures at 850 hPa exceeding 30 °C in SBA were observed on September 5–6 (Fig. 7c, d).

On September 6 2020, when record-breaking temperatures were reported in SBC, the thermal low pressure observed over Baja Californian and NW Mexico was about 1008 hPa, similarly to the observations on July 6 2018 (compare with Fig. 2). The most remarkable difference between the two events was the position of the anti-cyclone over the Pacific Ocean and the relatively weaker MSLP gradient affecting the SBA area. The minimum MSLP differences were -3.6 hPa (KSBA minus KBFL), and -3.3 hPA (KSBA minus KSMX) (see supplemental Figure S3b). They were both smaller than during the July 2018 event and did not exceed the 95th percentiles (Fig. S4).

4.3. Mesoscale forcings

4.3.1. Observations

Fig. 8 show observed diurnal cycles of temperature, winds and T_d from stations. All stations reached their highest temperature in the early-to-mid-afternoon, consistent with the climatology (Zigner et al., 2021). Temperatures were highest in the SYV stations (LPOC1, KIZA) reaching 48.3 °C (118.9°F) and 47.0 °C (116.6°F), resp., (Fig. 8a). Similarly to July 6 2018, the west–east temperature gradient in the SYV reached about 15 °C. This temperature gradient in the SYV was largely driven by the increase of temperatures within the valley (KIZA,

Same as Table 2 but for September 6 2020. See Fig. S6 in supplemental material for a spatial map.

Station	Elevation (m)	<i>T_{max}</i> (°C)	T _{max} (°F)	T_d (°C)	RH (%)	Wind (gust) (m s ⁻¹)	Wdir (°N)	Time (PDT)
LPOC1	299	48.3 (100.0)	118.9	6.2	8	0.9 (4.9)	241	15:35
KIZA	205	47.0 (100.0)	116.6	4.7	7.7	3.1 (-)	210	13:55
MPWC1	455	46.1 (100.0)	115.0	7.7	10	2.7 (4.5)	213	15:06
RHWC1	447	46.1 (100.0)	115.0	9.1	11	2.7 (4.9)	165	14:06
SBVC1	230	44.4 (100.0)	111.9	10.2	13	2.2 (4.0)	232	12:24
FGMC1	970	43.3 (100.0)	109.9	4.1	9	1.3 (6.2)	220	14:35
MTIC1	494	43.9 (99.9)	111.0	9.8	13	3.6 (5.4)	214	14:47
MOIC1	87	40.6 (99.9)	105.1	14.2	21.0	0.9 (2.2)	217	12:07
KSMX	74	38.0 (99.9)	100.4	16.2	27.5	3.6 (-)	320	13:00
KSBA	3	34.0 (99.9)	93.2	16.1	34.2	2.6 (-)	250	14:00
KVBG	112	33.8 (99.9)	92.8	15.0	32.3	2.1 (-)	340	10:58
KLPC	27	33.0 (99.9)	91.4	17.1	38.6	4.1 (-)	230	12:00
KBFL	155	40.0 (99.6)	104.0	16.3	24.7	5.1 (-)	300	15:00

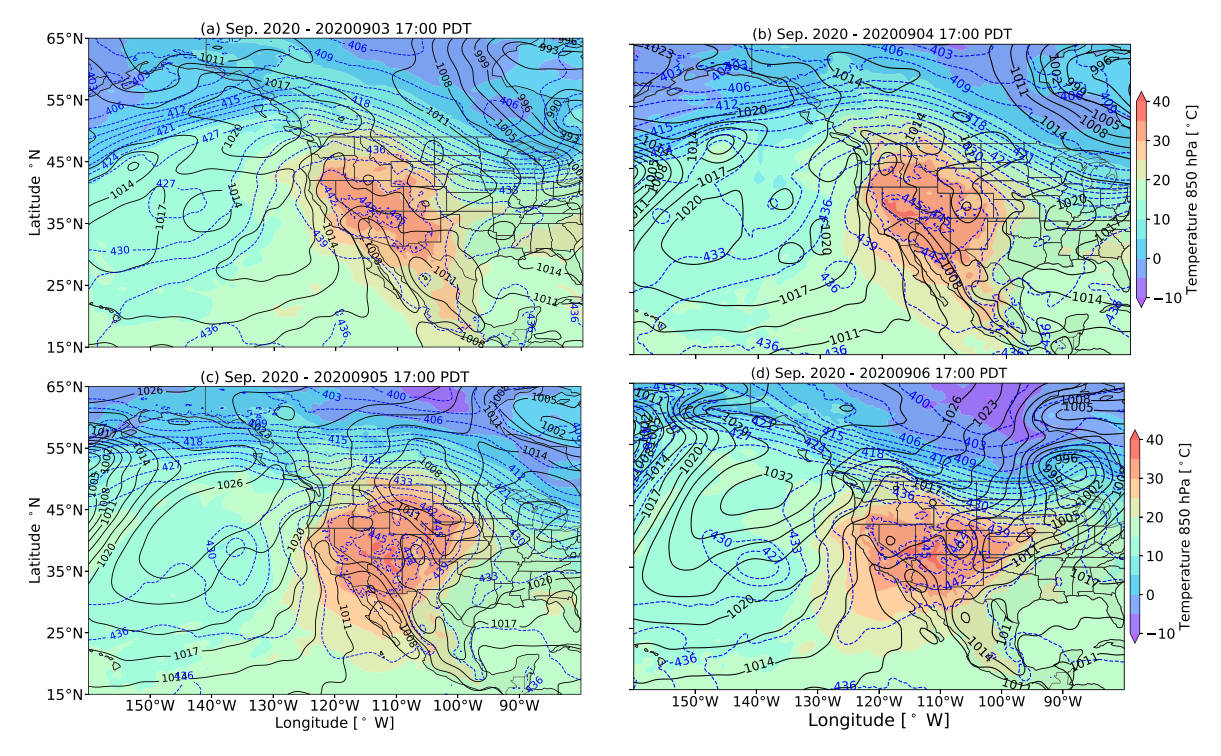


Fig. 7. Same as Fig. 2 but for the days leading up to the September 6 2020 event.

LPOC1 stations) combined with a decrease of temperatures at the coast (KVBG) due to sea breeze, as evidenced by the combined increase of winds (Fig. 8b) and T_d at this site starting around 11:00 PDT (Fig. 8c).

Even though the temperatures at the SYM slope stations RHWC1 and SBVC1 were lower than in the SYV (46.1 °C and 44.4 °C, resp.), they still reached all-time records (Fig. 8d). The stations in and around the SYM exhibited an increase in winds from 18:00 PDT, with strongest winds at MTIC1 (13.9 m s⁻¹) followed by RHWC1 (11.6 m s⁻¹) (Fig. 8e). Consequently, temperatures at these locations remained relatively high during early evening (Fig. 8d), which contrasts the other stations that showed a gradual decrease in temperatures and winds throughout the late afternoon and evening (Fig. 8d,e). The relatively high temperatures in the early evening were possibly resulting from a combination of turbulent mixing of residual air, air mass change, and compressional heating (Whiteman, 2000). Around 22:00 PDT, the MOIC1 and SBVC1 stations revved back to 40 °C for a short period of time (Fig. 8d). Notice that this temperature was close to T_{max} . These temperature jumps were accompanied by enhanced wind gusts around the same time (not shown). The MOIC1 and SBVC1 stations are situated at the lowest elevations of the SYM slopes (Table 3), and are closer to the ocean, making the effects of adiabatic warming

and SSMBL presence more prominent compared to other stations at higher elevations (RHWC1, MTIC1) (Carvalho et al., 2020). The sudden decrease in T_d at the MOIC1 and SBVC1 stations nevertheless indicates the intrusion of a much drier air mass, providing evidence of mountain waves for driving temperature shifts during the night (Fig. 8f).

4.3.2. WRF simulations

Comparisons between observations and simulations are shown in supplemental material Figure S7. We investigate simulations of winds and temperature to further understand prevailing mechanisms associated with the observed diurnal cycles. At 10:00 PDT, winds in the SYV were weak (Fig. 9a), typical for flat terrain at this time (Whiteman, 2000). Moderately strong NW winds were present off the coast near Point Conception, which is consistent with the climatology of the region (Dorman and Winant, 2000; Zigner et al., 2021), but weaker than during July 6 2018 (Section 3.3). At 12:00 PDT, winds over land increased in strength, and were mostly directed upslope and upvalley (Fig. 9b). This follows the general transition time from the down- to upvalley flow in the area conducive to thermally-driven gradients (Zigner et al., 2021). Simulated temperatures in the SYV were as high as 40 °C at this time, and differences between coastal and inland sites increased, similar to the July 6 2018 case.

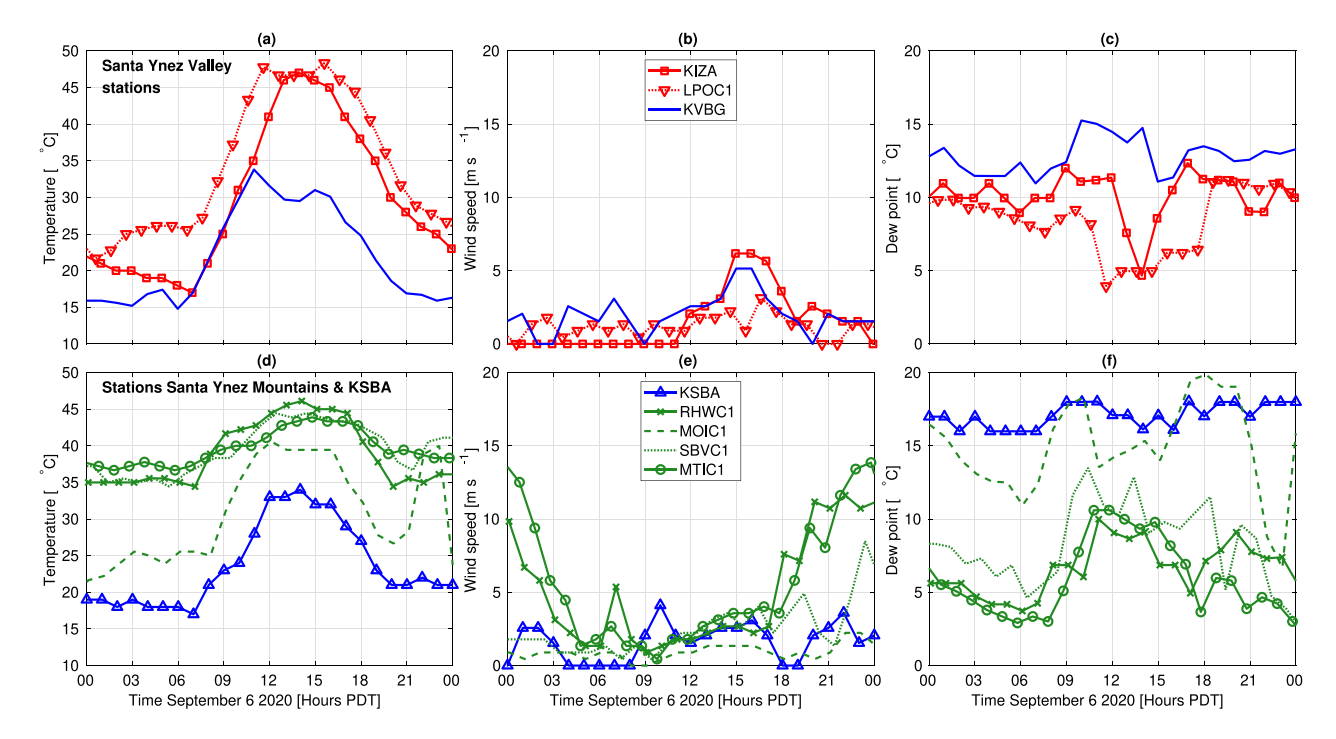


Fig. 8. Same as Fig. 3 but for September 6 2020.

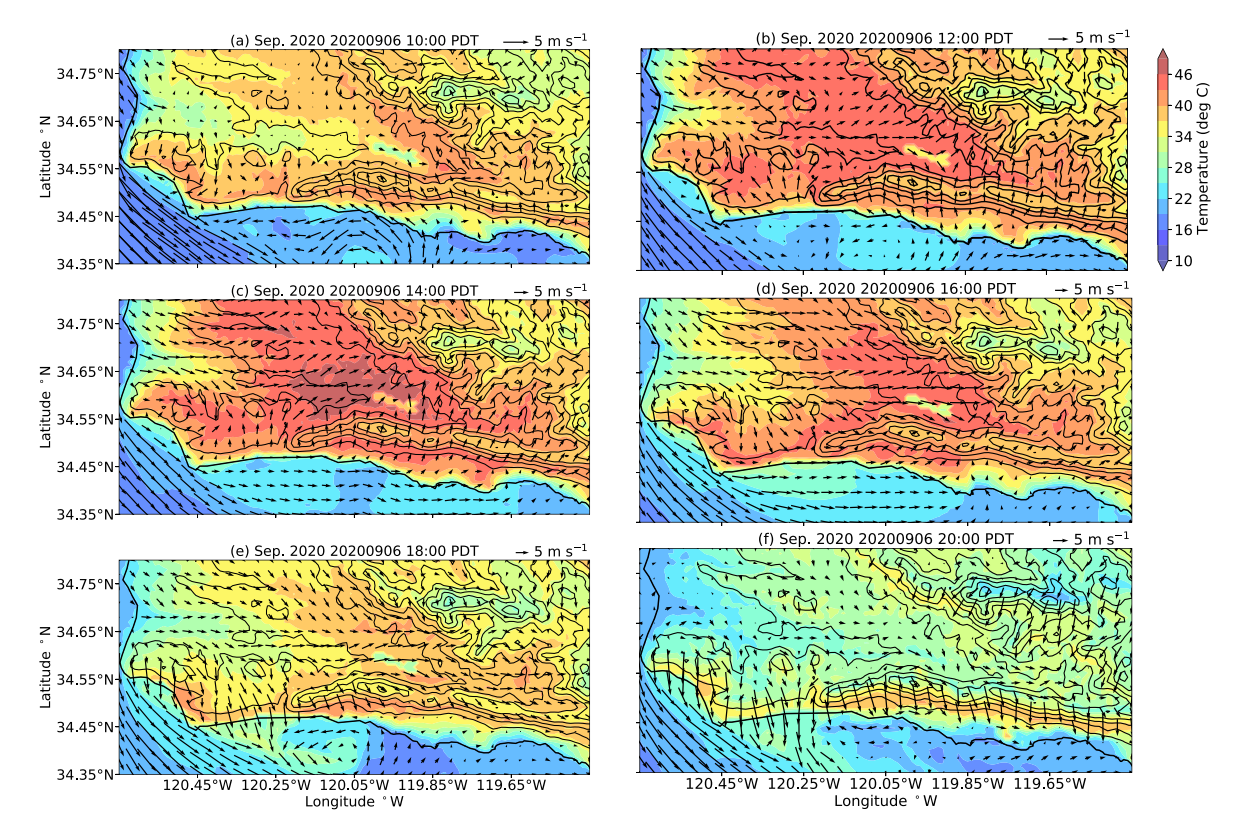


Fig. 9. Same as Fig. 4 but for the September 6 2020 event. Note the scale of the quivers is 5 m s $^{-1}$.

At 14:00 PDT, air temperatures ranged from 43 °C on the south-facing side of the SYM to above 46 °C in the SYV in simulations (Fig. 9c). On the SYM south-facing slopes, winds remained weak (5 m s $^{-1}$ or less) and mostly upslope. Temperatures in most locations decreased from around 14:00 PDT, and winds remained similar in strength and direction (Figs. 9d), similar to observations. While surface cooling continued at 18:00 PDT, winds weakened in most locations

(Fig. 9e), except for the south-facing slopes of the SYM, where winds have shifted from up- to downslope (Fig. 9e). The latter shift was most prominent in the western portion of the SYM at this time (west of 119.85°W). A combination of CBL development in the SYV, thermally-driven upslope winds on the south-facing side of the SYM, and the relatively weak MSLP gradient likely prevented earlier enhancement of these winds on the south-facing slopes of the SYM (Duine et al., 2021).

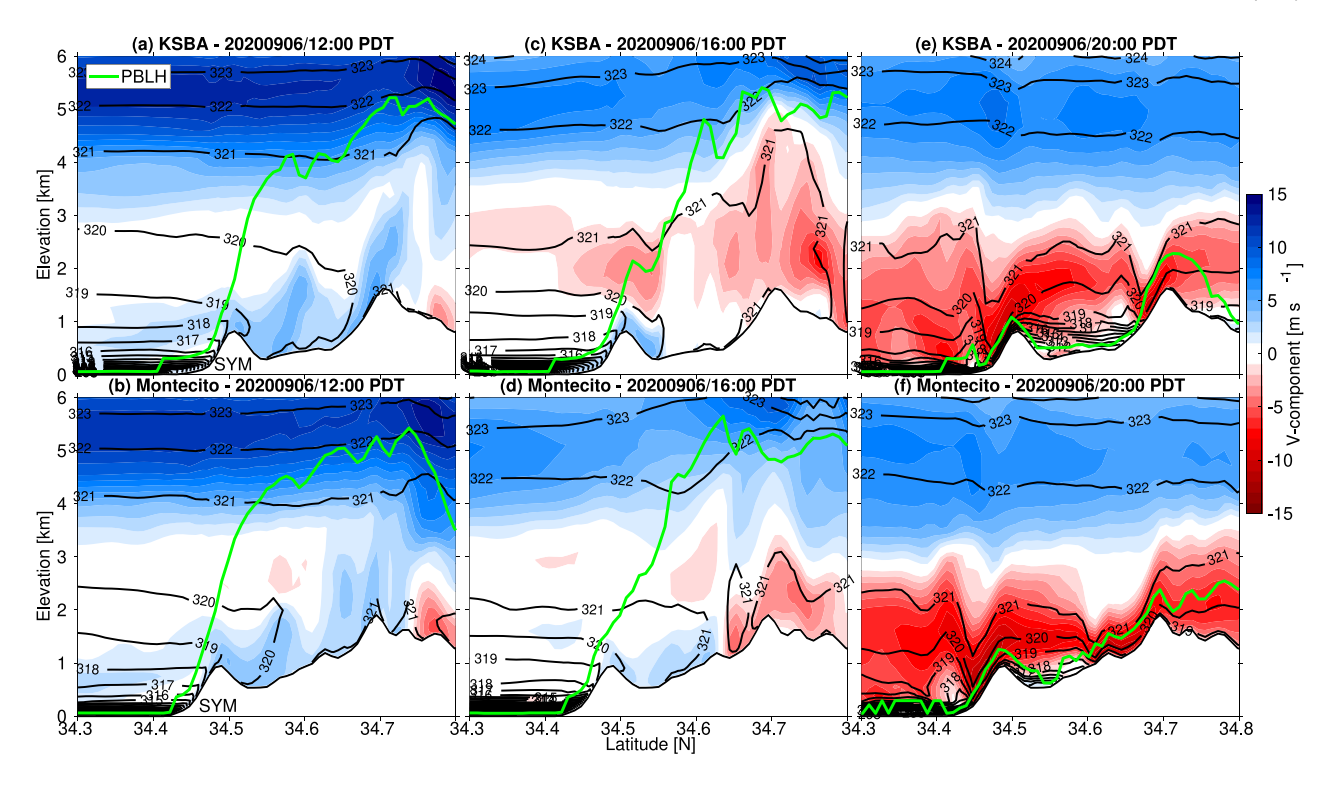


Fig. 10. Same as Fig. 5 but for the September 6 2020 event. Note that upper boundaries are at 6 km.

The MSLP gradient was, however, strong enough to force stronger downslope winds on the south-facing slopes of the SYM (Fig. 9f), a pattern that typically arises after sunset when solar surface heating is absent (Jones et al., 2021; Zigner et al., 2021), and confirming the differences in the observed temperatures and winds in Fig. 8d,e.

Cross sections of θ_v , V-component and PBL height on September 6 2020 showed remarkable differences between southern SYM and the SYV. Both KSBA and Montecito cross-sections indicate the presence of a SSMBL south of the SYM at noon and 16:00 (Fig. 10a–d). In contrast to July 6 2018, the stable core in the SYV was eroded before 11:00 PDT (not shown). The CBL depth over the SYV exceeded 4 km msl already at noon (Fig. 10a, b), and remained high even at 16:00 PDT (Fig. 10c, d). Above the CBL, at around 4 km msl, winds were oriented on a southerly direction (Fig. 10). Similar to July 6 2018, these were driven by large-scale synoptic forcing in the mid-troposphere at the 500 hPa level (Fig. 7). The afternoon CBL was extraordinarily high for the time of year, which may have been a combination of residual heat build-up and warm-air advection, processes that are typical to heatwaves (Miralles et al., 2014), and their combination may lead to early development of very deep CBLs (Lin et al., 2018).

By 20:00 PDT, the CBL had collapsed, and the level at which the cross-barrier wind component (V-component) reaches zero lowered to about 3 km msl (Fig. 10e, f), similar to the July 6 2018 case. Northerly winds approached the SRM and SYM due to negative MSLP gradient over the SBA area. The downslope winds remained relatively weak, and were mostly focused on the upper portions of the SYM, and impacted the eastern portion of the mountains, evidenced by temperature jumps in MOIC1 and SBVC1 as noted before.

4.3.3. Upper-air sounding observations

Fig. 11 shows the 62-yr radiosonde temperature distribution during September at Vandenberg (KVBG) at 00:00 UTC (17:00 PDT), and emphasizes the extreme heat in the lowest 4 km. The observed temperatures at 850 hPa and 700 hPa were 16.0 and 31.4 °C, respectively, both values exceeding the 99th percentile (Fig. 11a, b). The observed 500 hPa temperature was -7.5 °C, a value close to the median value of -7.7 °C for September (Fig. 11c). If conditions for

Sundowner winds and respective mountain waves were present, the adiabatic transport of air parcels from 850 hPa would result in surface temperatures downslope of the SYM reaching 46.1 °C. However, T_{max} was observed during mid-afternoon hours, when strong downslope winds were absent. Thus, a combination of high temperatures due to warm air advection and vigorous CBL growth development in the SYV, typical of desert regions (Stull, 1988), resulted in the extreme temperatures that were observed on September 6, 2020. In fact, this was a large-scale heatwave event that affected other regions of California, as shown by temperatures observed much farther north in Bakersfield (KBFL station), where the observed T_{max} exceeded its 99.6th percentile (Table 3).

5. Wildfire index in Santa Barbara County

We discuss the importance of the July 6 2018 and September 6 2020 heatwaves in the context of the FFWI (Eq. (1)). For this discussion we selected a few stations on the southern slopes of the SYM that had observations for at least 5 years (see Table 1). We plotted FFWI (colors) as a function of temperature T (horizontal axis), wind speed (vertical axis) and RH (blue lines) (Fig. 12). The distribution of FFWI was then compared to the observed values during the two heatwaves (Fig. 12, symbols). FFWI greater than 25 have been related to high fire risk in chaparral ecosystems (Moritz et al., 2010), the predominant land cover on the slopes of the SYM. Diagrams obtained for other stations, including comparison with climatological means from simulations, are shown in the supplemental figures (Figs. S8-S9).

Because FFWI is sensitive to air mass differences in temperature and humidity, the same wind speeds can result in distinct FFWI (Zigner et al., 2021). This is demonstrated by comparing RHWC1 and MTIC1 stations (Fig. 12a, b). For example, on average, for a temperature of 20 °C and a wind speed of 15 m s⁻¹, we find FFWI values around 55 for RHWC1 (Fig. 12a), but approaching 80 at MTIC1 (Fig. 12b). The dependency on humidity when observing high winds also depends on the geographical position of the station. For instance, strong winds (say, around 15 m s⁻¹) at RHWC1 (western SYM) have been associated with RH ranging from above 80% to below 40%. Conversely, strong

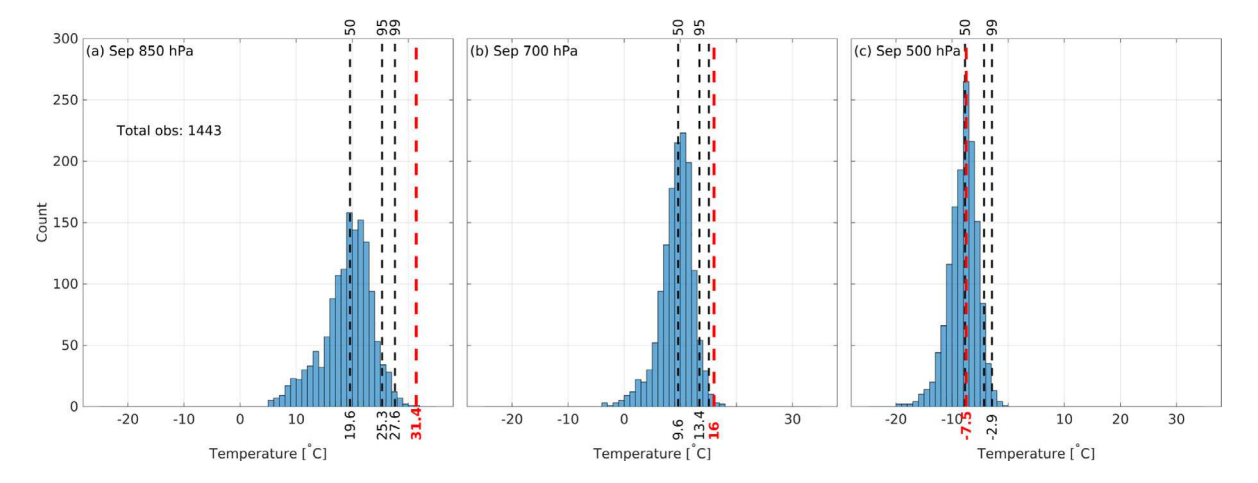


Fig. 11. Same as Fig. 6, but for September 6 2020 event and including September radiosonde climatology at KVBG.

winds at MTIC1 (eastern SYM) have been typically related to lower RH, ranging from around 40% to below 20%. Higher RH during Sundowners have been commonly observed on the western portion of the SYM and have been attributed to moisture advection by the predominant NW winds (Carvalho et al., 2020; Zigner et al., 2021; Duine et al., 2021).

Additionally, the FFWI-diagrams allow the identification of previously observed extreme FFWI events. For instance, FFWIs of almost 100 (extreme wildfire risk) have been observed at MTIC1 (Fig. 12b), whereas historical extreme values at RHWC1 do not exceed 90 (Fig. 12a). Although the FFWI climatology provides a good indication of potential fire risks, the caveat is that they depend on the record length, elevation and exposure of the station to extreme winds, among other factors. While some stations situated in the SYM lee slope indicate similar climatology (RHWC1, MPWC1 and SBVC1, Fig. 12a, c, d), they differ considering extremes. For example, winds up to 20 m s⁻¹ have been observed at RHWC1, whereas in both MPWC1 and SBVC1 the maximum reported winds were about 15 m s⁻¹. Note that we have not included gusts in this analysis, which would likely result in more extreme values.

To place the two heatwaves into the historical wildfire risk context, we overlaid hourly observations of wind and temperature for the July 6 2018 and September 6 2020 heatwave events in the FFWI-diagrams. In most locations in the SYM lee slopes (RHWC1, MTIC1, MPWC1, SBVC1), the observations during the heatwave events were at the far end of their respective FFWI distribution (Fig. 12a-d). Between the two extreme events, the July 6 2018 heatwave along with a Sundowner event (black triangles) stands out for higher values of FFWI for each station. Clearly, the combination of strong winds and relatively high temperatures drove FFWI to peak values at RHWC1, MPWC1 and SBVC1 stations during this event (Fig. 12a, c, d). Although the temperatures were generally higher during the September 6 2020 event (marked in red), this day showed remarkably lower values of FFWI. Only where winds exceeded 10 m s⁻¹, the FFWI exceeded 50.

Contrastingly, coastal KSBA and valley (KIZA) stations differ in behavior compared to stations on the slopes of the SYM. At KSBA, the values for FFWI remained below 30 and were mostly driven by the higher temperatures in both events with the September heatwave exhibiting remarkably higher values due to higher temperatures (Fig. 12e). For the valley station KIZA, the observed FFWI was relatively low for both cases as a consequence of weak winds (Fig. 12f). Nevertheless, while July 6 2018 had relatively low temperatures (compared to September 6 2020) in the SYV, winds were higher driving FFWI to above 50 for one single hour. Note that MSLP differences were close to half of the values of July 6 2018 Sundowner event during the September 6 2020 event (Fig. S3). These examples point to potential wildfire risk for communities living in the Santa Barbara County. As the climate

warms and the number of heatwaves increase (Perkins-Kirkpatrick and Gibson, 2017), weather conditions conducive of cross-mountain winds leading to Sundowners, similarly to July 2018, can significantly increase wildfire risks (Keellings and Moradkhani, 2020). If significant pressure gradients were forcing a Sundowner event on September 6 2020, FFWI values would have been 'off the charts' for each station. No historical observation has shown this combination yet, but it is important to note that winds exceeding 15 m s⁻¹ have been recorded in the past decades.

6. Conclusions

Two heatwave events affecting Santa Barbara County, their mechanisms and impact on wildfire risk were discussed. To investigate the extreme nature of these events we used a combination of observations and simulations, including surface stations with records (5 to 20 yrs), radiosoundings (62 yr), and regionally downscaled simulations at 1 km grid spacing (32 yr). While both extreme events were different in nature and associated with distinct forcings, they resulted in record-breaking temperatures in many locations and unprecedented wildfire risks.

The first heatwave occurred on July 6 2018 during which one station recorded an all-time maximum temperature. On that day, we found that a combination of strong Sundowner winds and high temperatures (exceeding the 95th percentile in many locations) led to critical fire weather conditions in the Santa Ynez Mountains (SYM). Remarkably, high temperatures were observed early evening associated with strong Sundowners and mountain waves that caused adiabatic warming and drying of the lower troposphere. Lee slope jet accelerations resulted from the extreme MSLP gradients over the area, combined with the profile of atmospheric stability and the presence of a mean-state critical layer upstream of the SYM. Consequently, a lower slope (87 m) station on the eastern south-facing slopes of the SYM (MOIC1) broke all-time temperature record in the evening (42.2 °C, 108.0°F), while others exceeded their respective 99.9th percentiles. Maximum observed winds reached about 16.1 m $\rm s^{-1}$ (RHWC1), while gusts reached 23.7 m $\rm s^{-1}$ (SBVC1). The wildfire that erupted on the SYM south-facing slopes, known as the Holiday fire, remained relatively small in size thanks to coordination between NWS forecasts and the operations developed by the Santa Barbara County Fire Department (Mark Johnson, chief meteorologist, NWS/LA Oxnard office, personal communication).

The second heatwave investigated here occurred on September 6 2020. This heatwave broke all temperature records for ten surface stations used in this study, while four others exceeded the 99.9th percentile. The highest temperature was recorded at LPOC1 (48.3 °C, 118.9°F), located in the narrowest parts of the SYV. This event broke a monthly record of 62-yr radiosounding temperatures at 850 hPa recorded in the nearby Vandenberg site. These records were related to

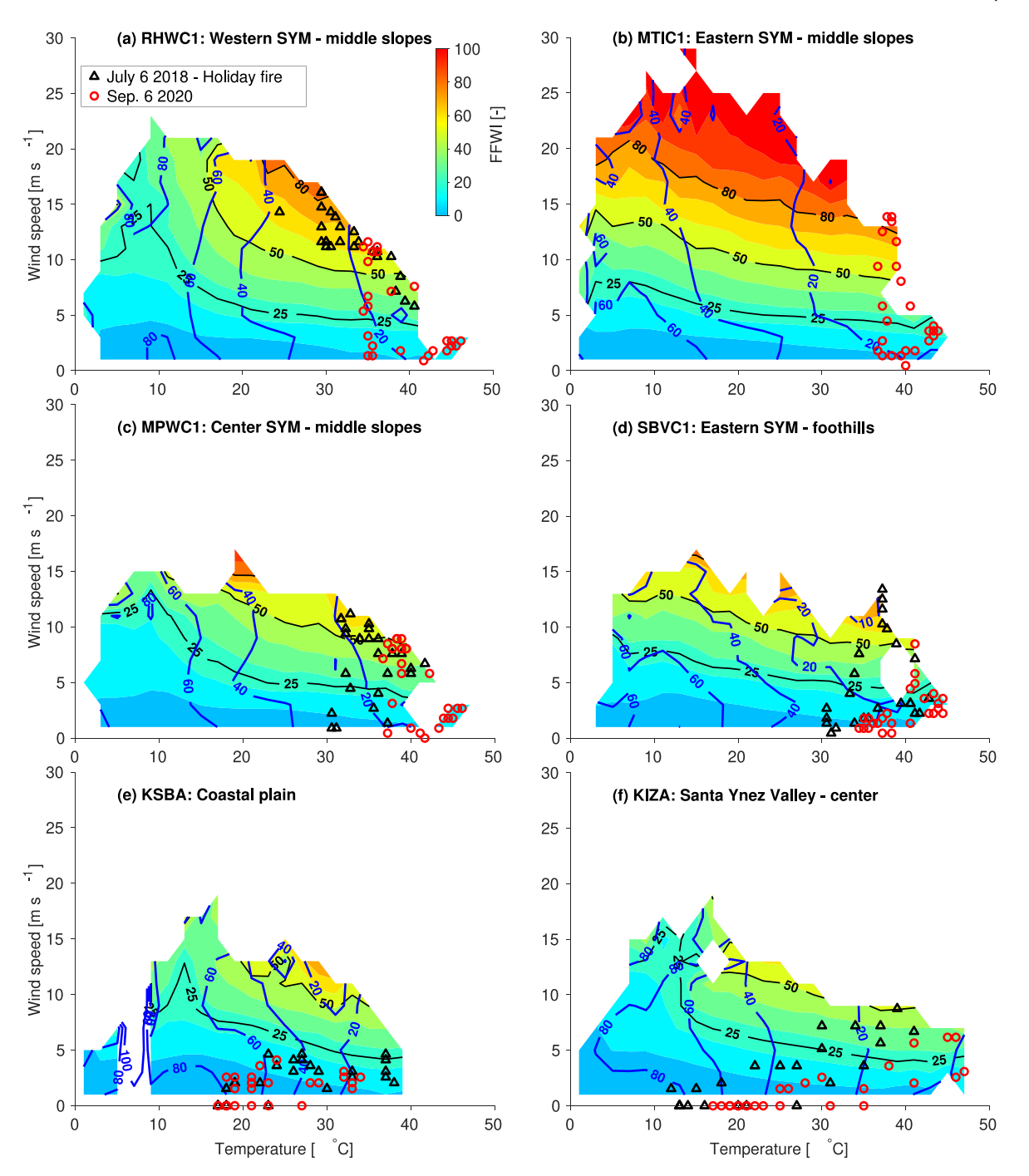


Fig. 12. FFWI (colored contours) and RH (blue contours)-averaged diagrams as a function of temperature and winds. Bins for temperature and winds were 2 °C and 2 m s⁻¹, resp. Each diagram shows the hourly observations of temperature and wind to stress the extremity of the events. Legend and colorbar provided in (a) applies to all panels. See Fig. 1 for the station locations. (For interpretation of the references to color in this figure legend, the reader is referred to the web version of this article.)

a heatwave affecting larger parts of the western US that persisted for a few days, allowing tropospheric heat to build up in the study area. Winds in the area remained relatively weak throughout the event.

This study proposes a novel diagram to place the heatwave extremes into historical context. Based on the fire risk indicated by the FFWI, the July 6 2018 presented a higher fire risk than the September 6 2020 due to the combination of strong winds and high temperatures occurring in the evening. Despite the excessive temperatures reported on September 6 2020, less extreme values for FFWI were observed and simulated, as a consequence of the weaker winds. An unprecedented and severe wildfire risk scenario would be possible if similar MSLP differences had occurred as during the July 6 2018 event. As the expected frequency

of heatwaves increases in a warming planet, unprecedented wildfire risks may be observed in the complex terrain of California. Our research demonstrates that understanding atmospheric conditions conducive to downslope winds such as Sundowner winds during heatwaves is critical for reliable predictions of severe wildfire risks for populated areas. This study thereby contributes to evaluate these risks in Santa Barbara, and can be insightful for heatwave and wildfire mitigation purposes in a warmer climate.

CRediT authorship contribution statement

Gert-Jan Duine: Conceptualization, Methodology, Software, Formal analysis, Investigation, Data curation, Writing – original

draft, Writing – review & editing, Visualization. Leila M.V. Carvalho: Conceptualization, Methodology, Validation, Investigation, Resources, Writing – review & editing, Supervision, Project administration, Funding acquisition. Charles Jones: Conceptualization, Methodology, Software, Validation, Investigation, Resources, Writing – review & editing, Project administration, Funding acquisition.

Declaration of competing interest

The authors declare that they have no known competing financial interests or personal relationships that could have appeared to influence the work reported in this paper.

Acknowledgments

The radiosounding data at KVBG were obtained from the Integrated Global Radiosonde Archive (IGRA) through ftp://ftp.ncdc.noaa.gov/. Station data were obtained through the Mesowest database (Horel et al., 2002). This research was supported by the Integrative and Collaborative Education and Research (ICER), USA program (ICER-1664173), and the Physical and Dynamic Meteorology program (NSF-1921595) from the National Science Foundation, USA. The authors thank NWS/LOX Mark Johnson and David Gomberg for the provided details on the Holiday Fire event.

Appendix A. Supplementary data

Supplementary material related to this article can be found online at https://doi.org/10.1016/j.wace.2022.100482.

References

- Adams, R.E., Lee, C.C., Smith, E.T., Sheridan, S.C., 2020. The relationship between atmospheric circulation patterns and extreme temperature events in North America. Int. J. Clim. 41 (1), 92–103.
- Blier, W., 1998. The sundowner winds of Santa Barbara, California. Wea. Forecasting 13 (3), 702–716.
- Cannon, F., Carvalho, L.M., Jones, C., Hall, T., Gomberg, D., Dumas, J., Jackson, M., 2017. WRF simulation of downslope wind events in coastal Santa Barbara county. Atmos. Res. 191, 57–73.
- Cao, Y., Fovell, R.G., 2018. Downslope windstorms of San Diego county. Part II: Physics ensemble analyses and gust forecasting. Wea. Forecasting 133 (4), 539–559.
- Carvalho, L.M., Duine, G.-J., Jones, C., Zigner, K., Kane, H., Gore, C., Bell, G., Gamelin, B., Gomberg, D., Hall, T., Johnson, M., Dumas, J., Boldt, E., Hazard, R., Enos, W., 2020. The sundowner winds experiment (SWEX) pilot study: Understanding downslope windstorms in the santa ynez mountains, Santa Barbara, California. Mon. Wea. Rev. 148 (4), 1519–1539.
- Dorman, C., Winant, C., 2000. The structure and variability of the marine atmosphere around the Santa Barbara channel. Mon. Wea. Rev. 128 (2), 261–282.
- Dosio, A., Mentaschi, L., Fischer, E.M., Wyser, K., 2018. Extreme heat waves under 1.5 $^{\circ}$ c and 2 $^{\circ}$ c global warming. Environ. Res. Lett. 13 (5), 054006.
- Duine, G.-J., Carvalho, L.M., Jones, C., Zigner, K., 2021. The effect of upstream orography on the onset of sundowner winds in coastal Santa Barbara, CA. J. Geophys. Res.: Atmos. 126 (8), e2020JD033791.
- Duine, G.-J., Jones, C., Carvalho, L.M., Fovell, R.G., 2019. Simulating sundowner winds in coastal Santa Barbara: Model validation and sensitivity. Atmosphere 10 (3), 155.
 Durran, D.R., 1990. Mountain waves and downslope winds. In: Atmospheric Processes
- over Complex Terrain. Springer, pp. 59–81. Feng, S., Wu, X., Hao, Z., Hao, Y., Zhang, X., Hao, F., 2020. A database for
- Feng, S., Wu, X., Hao, Z., Hao, Y., Zhang, X., Hao, F., 2020. A database for characteristics and variations of global compound dry and hot events. Weather Clim. Extrem. 30, 100299.
- Fosberg, M.A., 1978. Weather in wildland fire management: The fire weather index. In: Proc. Conf. on Sierra Nevada Meteorology. Lake Tahoe, CA, Amer. Meteorol. Soc., pp. 1–4.
- Gershunov, A., Cayan, D.R., Iacobellis, S.F., 2009. The great 2006 heat wave over California and nevada: Signal of an increasing trend. J. Clim. 22 (23), 6181–6203.
- Goodrick, S.L., 2002. Modification of the fosberg fire weather index to include drought. Int. J. Wildland Fire 11 (4), 205–211.
- Grotjahn, R., Black, R., Leung, R., Wehner, M.F., Barlow, M., Bosilovich, M., Gershunov, A., Gutowski, W.J., Gyakum, J.R., Katz, R.W., et al., 2016. North American Extreme temperature events and related large scale meteorological patterns: A review of statistical methods, dynamics, modeling, and trends. Clim. Dyn. 46 (3), 1151–1184.

- Grubišić, V., Serafin, S., Strauss, L., Haimov, S.J., French, J.R., Oolman, L.D., 2015.
 Wave-induced boundary layer separation in the lee of the medicine bow mountains.
 Part II: Numerical modeling. J. Atmos. Sci. 72 (12), 4865–4884.
- Hersbach, H., Bell, B., Berrisford, P., Hirahara, S., Horányi, A., Muñoz-Sabater, J., Nicolas, J., Peubey, C., Radu, R., Schepers, D., et al., 2020. The ERA5 global reanalysis. Q. J. Roy. Meteor. Soc. 146 (730), 1999–2049.
- Horel, J., Splitt, M., Dunn, L., Pechmann, J., White, B., Ciliberti, C., Lazarus, S., Slemmer, J., Zaff, D., Burks, J., 2002. Mesowest: Cooperative mesonets in the western United States. Bull. Am. Meteorol. Soc. 83 (2), 211–226.
- Jones, C., Carvalho, L.M., Duine, G.-J., Zigner, K., 2021. Climatology of sundowner winds in coastal Santa Barbara, California, based on 30 yr high resolution WRF downscaling. Atmos. Res. 249, 105305.
- Jones, C., Fujioka, F., Carvalho, L.M., 2010. Forecast skill of synoptic conditions associated with santa ana winds in Southern California. Mon. Wea. Rev. 138 (12), 4528-4541.
- Jyoteeshkumar reddy, P., Sharples, J.J., Lewis, S.C., Perkins-Kirkpatrick, S.E., 2021. Modulating influence of drought on the synergy between heatwaves and dead fine fuel moisture content of bushfire fuels in the southeast Australian region. Weather Clim. Extrem. 31, 100300. http://dx.doi.org/10.1016/j.wace.2020.100300, URL https://www.sciencedirect.com/science/article/pii/S2212094720303133.
- Keellings, D., Moradkhani, H., 2020. Spatiotemporal evolution of heat wave severity and coverage across the United States. Geophys. Res. Lett. 47 (9), e2020GL087097.
- Lin, Z., Bo, H., Shihua, L., Lijuan, W., Xianhong, M., Zhaoguo, L., 2018. The different influence of the residual layer on the development of the summer convective boundary layer in two deserts in northwest China. Theor. Appl. Climatol. 131 (3), 877–888.
- Miralles, D.G., Teuling, A.J., Van Heerwaarden, C.C., De Arellano, J.V.-G., 2014. Megaheatwave temperatures due to combined soil desiccation and atmospheric heat accumulation. Nat. Geosci. 7 (5), 345–349.
- Moon, J.-Y., Wang, B., Ha, K.-J., 2011. ENSO regulation of MJO teleconnection. Clim. Dyn. 37 (5–6), 1133–1149.
- Moritz, M.A., Moody, T.J., Krawchuk, M.A., Hughes, M., Hall, A., 2010. Spatial variation in extreme winds predicts large wildfire locations in chaparral ecosystems. Geophys. Res. Lett. 37 (4).
- Murray, A.T., Carvalho, L., Church, R.L., Jones, C., Roberts, D., Xu, J., Zigner, K., Nash, D., 2021. Coastal vulnerability under extreme weather. Appl. Spat. Anal. Polic. 14 (3), 497–523.
- Nakanishi, M., Niino, H., 2006. An improved Mellor-Yamada level-3 model: Its numerical stability and application to a regional prediction of advection fog. Bound-Lay. Meteorol. 119 (2), 397–407.
- Nash, D., Carvalho, L.M., 2020. Brief communication: An electrifying atmospheric riverunderstanding the thunderstorm event in Santa Barbara county during March 2019. Nat. Hazard. Earth Syst. 20 (7), 1931–1940.
- Oakley, N.S., Cannon, F., Munroe, R., Lancaster, J.T., Gomberg, D., Ralph, F.M., 2018.
 Brief communication: Meteorological and climatological conditions associated with the 9 january 2018 post-fire debris flows in Montecito and Carpinteria, California, USA. Nat. Hazard. Earth Syst. 18 (11), 3037–3043.
- Ostro, B.D., Roth, L.A., Green, R.S., Basu, R., 2009. Estimating the mortality effect of the july 2006 California heat wave. Environ. Res. 109 (5), 614–619.
- Pellizzaro, G., Cesaraccio, C., Duce, P., Ventura, A., Zara, P., 2007. Relationships between seasonal patterns of live fuel moisture and meteorological drought indices for Mediterranean shrubland species. Int. J. Wildland Fire 16 (2), 232–241.
- Perkins-Kirkpatrick, S., Gibson, P., 2017. Changes in regional heatwave characteristics as a function of increasing global temperature. Sci. Rep. UK 7 (1), 1–12.
- Perkins-Kirkpatrick, S., Lewis, S., 2020. Increasing trends in regional heatwaves. Nature Commun. 11 (1), 1–8.
- Robine, J.-M., Cheung, S.L.K., Le Roy, S., Van Oyen, H., Griffiths, C., Michel, J.-P., Herrmann, F.R., 2008. Death toll exceeded 70,000 in europe during the summer of 2003. C. R. Biol. 331 (2), 171–178.
- Skamarock, W.C., Klemp, J.B., 2008. A time-split nonhydrostatic atmospheric model for weather research and forecasting applications. J. Comput. Phys. 227 (7), 3465–3485.
- Stull, R.B., 1988. An Introduction to Boundary Layer Meteorology. Kluwer Academic Publishers, p. 666.
- Sukup, S., 2013. Extreme northeasterly wind events in the hills above Montecito, California. In: Western Region Technical Attachment NWS WR-1302. National Weather Service Western Region, Salt Lake City, UT.
- Sun, Q., Miao, C., Hanel, M., Borthwick, A.G., Duan, Q., Ji, D., Li, H., 2019. Global heat stress on health, wildfires, and agricultural crops under different levels of climate warming. Environ. Int. 128, 125–136.
- Sutanto, S.J., Vitolo, C., Di Napoli, C., D'Andrea, M., Van Lanen, H.A., 2020. Heat-waves, droughts, and fires: Exploring compound and cascading dry hazards at the pan-European scale. Environ. Int. 134, 105276.
- Tewari, M., Chen, F., Wang, W., Dudhia, J., LeMone, M., Mitchell, K., Ek, M., Gayno, G., Wegiel, J., Cuenca, R., 2004. Implementation and verification of the unified NOAH land surface model in the WRF model. In: 20th Conference on Weather Analysis and Forecasting/16th Conference on Numerical Weather Prediction. pp. 11–15.
- Thomas, N.P., Bosilovich, M.G., Marquardt Collow, A.B., Koster, R.D., Schubert, S.D., Dezfuli, A., Mahanama, S.P., 2020. Mechanisms associated with daytime and nighttime heat waves over the contiguous United States. J. Appl. Meteorol. Climatol. 59 (11), 1865–1882.

- Whiteman, C.D., 1982. Breakup of temperature inversions in deep mountain valleys: Part I. Observations. J. Appl. Meteorol. 21 (3), 270–289.
- Whiteman, C.D., 2000. Mountain Meteorology: Fundamentals and Applications. Oxford University Press.
- Williams, A.P., Abatzoglou, J.T., Gershunov, A., Guzman-Morales, J., Bishop, D.A., Balch, J.K., Lettenmaier, D.P., 2019. Observed impacts of anthropogenic climate change on wildfire in California. Earth's Future 7 (8), 892–910.
- Zeppetello, L.R.V., Battisti, D.S., Baker, M.B., 2022. The physics of heat waves: What causes extremely high summertime temperatures? J. Clim. 1–61.
- Zigner, K., Carvalho, L.M., Jones, C., Duine, G.-J., 2021. Extreme winds and fire weather in coastal Santa Barbara county, CA: An observational analysis. Int. J. Clim. 1–22. http://dx.doi.org/10.1002/joc.7262.
- Zigner, K., Carvalho, L., Peterson, S., Fujioka, F., Duine, G.-J., Jones, C., Roberts, D., Moritz, M., 2020. Evaluating the ability of FARSITE to simulate wildfires influenced by extreme, downslope winds in Santa Barbara, California. Fire 3 (3), 29.
- Zscheischler, J., Sillmann, J., Alexander, L., 2021. Introduction to the special issue: Compound weather and climate events. Weather Clim. Extrem. 100381.